processes

MDPI

Article

Multi-Condition Optimization of Cavitation Performance on a Double-Suction Centrifugal Pump Based on ANN and NSGA-II

Wenjie Wang [1], Yanpin Li [2], Majeed Koranteng Osman [1,3,*], Shouqi Yuan [1], Benying Zhang [1] and Jun Liu [4]

[1] National Research Center of Pumps, Jiangsu University, Zhenjiang 212013, China; wenjiewang@ujs.edu.cn (W.W.); shouqiy@ujs.edu.cn (S.Y.); ujs_zby@163.com (B.Z.)
[2] School of Water Conservancy, North China University of Water Resources and Electric Power, Zhengzhou 450045, China; liyanpin@ncwu.edu.cn
[3] Department of Mechanical Engineering, Wa Technical University, Wa XW-0547-6186, Ghana
[4] Shandong Shuanglun Co. Ltd., 6 Dongxin Road, Weihai 264203, China; liujun@shuanglun.cn
* Correspondence: mjk@ujs.edu.cn

Received: 25 July 2020; Accepted: 4 September 2020; Published: 10 September 2020

Abstract: Double-suction centrifugal pumps form an integral part of power plant systems in maintaining operational stability. However, there has been a common problem of achieving a better cavitation performance over a wider operating range because the traditional approach for impeller design often leads to the design effect not meeting the operational needs at off-design conditions. In addressing the problem, an optimization scheme was designed with the hub and shroud inlet angles of the double-suction impeller to minimize the suction performance at non-design flow conditions. A practical approach that speeds up the cavitation simulation process was applied to solve the experimental design, and a multi-layer feed forward artificial neural network (ANN) was combined with the non-dominated sorting genetic algorithm II to solve the multi-objective problem into three-dimensional (3D) Pareto optimal solutions that meet the optimization objective. At the design point, the suction performance was improved by 6.9%. At non-design flow conditions, the cavitation performance was improved by 3.5% at $1.2Q_d$ overload condition, 4% at $0.8Q_d$, and 5% at $0.6Q_d$. Additionally, there was significant reduction in the attached cavity distribution in the impeller and suction domains when the optimized model was compared to the original model at off-design points. Finally, the optimization established a faster method for a three-objective optimization of cavitation performance using ANN and 3D Pareto solutions.

Keywords: multi-condition optimization; cavitation performance; artificial neural networks (ANN); net positive suction head (NPSH); double suction

1. Introduction

In power plants, cooling water circulation pumps play an important role of distributing water to various parts of the plant to maintain operational stability. These pumps, mostly centrifugal pumps with double-suction impellers are usually operated continuously for long running hours for systems with large capacity demands due to their ability to deliver large flow rates at a constant head [1,2]. There is however a common problem of achieving a better cavitation performance over a wide operating range because traditional approach for impeller design often leads to the design effect not meeting the requirements at off-design conditions. This puts the downstream components at risk of being damaged since in most cases the flow passage gets blocked by the attached cavities [3,4]. In view of

this, the cooling water pumps are usually operated at rated design conditions to minimize the risk of cavitation which can lead to costly damage.

There has been an extensive literature on cavitation in centrifugal pump impellers over the past years, and these are readily available in open literature. Quite a number of these investigations predicted that there is some correlation between cavitation instabilities and changes in flow angle, the pressure gradient at cavity closure, as well as the flow rate and cavitation number [5,6]. More so, the unsteadiness in the pressure field vis-à-vis the rapid head-drop phenomenon that occurs during cavitation has been periodically analyzed in a centrifugal pump, and the reason for the head drop was attributed to the vortex generation in the cavitating region [7,8].

Pei [9] applied the L_9 (3^3) orthogonal design of experiments (DOE) and computational methods to improve the required net positive suction head (NPSHr) by 0.63 m. The relationship between the hub and shroud inlet angles have also been studied and established that a shroud blade angle of 30° improved cavitation performance [10]. The inverse design methodology has also been applied to parameterize the blade profile to improve suction performance and efficiency on a mixed flow pump impeller and diffuser [11]. Xu [12] performed a multi-objective optimization study using the Taguchi method. In his study, five design parameters of a centrifugal pump were sampled into 16 different impeller designs and optimized to improve design efficiency and cavitation performance.

Recently, there has been a shift from the single objective optimization methods to the application of genetic algorithms (GA) and surrogate models to find optimum global geometrical parameter combinations that can solve multi-objective optimization problems [13,14]. Jin [15] extensively reviewed the various surrogate models using their prediction accuracy, efficiency, and robustness, and concluded that for higher-order nonlinear problems, neural networks should be used. The application of artificial neural networks has gained much recognition in turbomachinery optimization. In centrifugal pumps, the radial bias neural network (RBNN) had the best prediction accuracy when compared with kriging and the response surface approximation model [16]. Moreover, Pei [13] carried out a multi-objective optimization on the inlet pipe shape of a vertical inline pump using artificial neural network (ANN) and multi-objective genetic algorithm (MOGA) to increase the efficiency over a wider range. Furthermore, the multi-layer neural network has been established to have a better prediction accuracy compared to the single-layer neural network [17].

Despite several optimization works on cavitation performance in centrifugal pumps, most of the studies have been focused on optimizing the inlet blade angle without focusing much on other impeller parameters such as the hub and shroud angles whose effect on cavitation performance has not been well researched. In addition, there is a common problem of achieving a better cavitation performance over a wider operating range in centrifugal pumps [18] since cavitation optimization studies have usually been centered on design and near-design flow conditions.

Therefore, in order to adapt to its multi-operating condition and broaden its non-cavitation operating range, an orthogonal scheme was designed to execute a multi-flow condition optimization for cavitation performance using a multi-layer feedforward neural network and the non-dominated sorting genetic algorithm II (NSGA-II). Since the traditional approach to predicting NPSHr is time consuming, a faster approach [19,20] was applied to reduce the simulation time during the optimization process. For this paper, a numerical anti-cavitation optimization design of the double-suction impeller was carried out at part load, the design point and at an overload condition to establish a set of optimum parameters that would best improve the suction performance at off-design flow conditions.

2. Optimization Procedure

Figure 1 shows the optimization procedure. The initial process was to sample the input bound variables based on an orthogonal design of experiment. Secondly, series of 3D model double-suction impellers were designed by bladegen in ANSYS 2019 R3 and CREO 5.0. ANSYS was adopted for the numerical simulations to obtain the objective function values, which was used to train the surrogate

models. The multi-objective problem was then solved to obtain 3D Pareto solutions, which were then verified by numerical simulation to determine the reliability of the optimization.

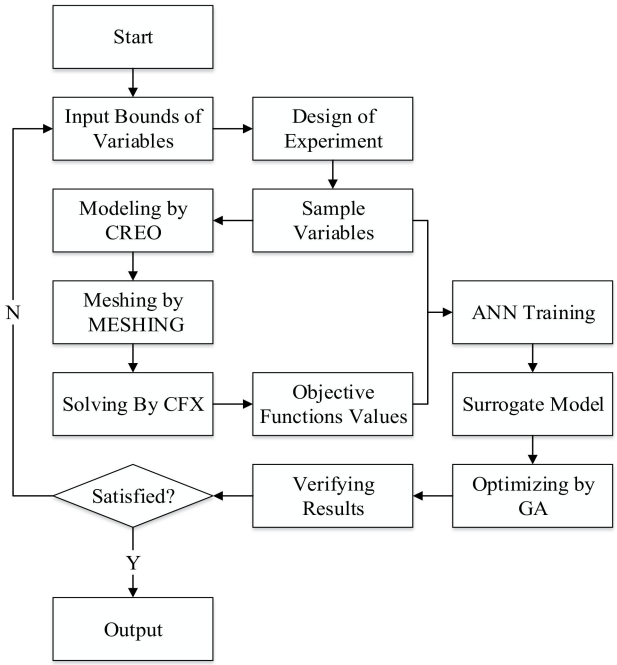

Figure 1. Flowchart of optimization process.

2.1. Objective Functions

During the optimization process of centrifugal pumps, the goals and targets are considered as significant indexes for performance evaluation. For this study, the NPSHr at three flow conditions were selected as the optimization targets. The objective function is to minimize the NPSHr at part loads ($0.8Q_d$), the nominal flow condition ($1.0Q_d$), and overload ($1.2Q_d$) flow conditions. These conditions are obtained by numerical calculations. The mathematical relation for NPSH is

$$NPSH = \frac{p - p_v}{\rho g} + \frac{{V_{in}}^2}{2g} \quad (1)$$

p and V_{in} represents static pressure and velocity at the pump inlet respectively, p_v is the vapor pressure, ρ is density, and g is the gravitational acceleration [21].

2.2. Design of Experiment

In deciding the optimization variables, the inlet diameter of the impeller, D_1, the impeller diameter at the outlet, D_2, the diameter of the hub D_h, and the blade width at outlet b_2 were held constant. This was to maintain the shape of the impeller due to space constrains of the suction and volute casing of the double-suction centrifugal pump. The choice of decision variables was limited to the blade inlet profile at hub and shroud. Three geometrical parameters, namely, hub inlet angle β_1 hub, middle inlet angle β_2 middle, and the shroud inlet angle β_3 shroud were selected as optimization variables. Each parameter was given a set of five values. Table 1 shows the decision variables and their set of values used for the parameterization. Orthogonal design of experiment was applied here to design the experimental scheme. From Table 1, there were 3 factors and 5 levels for the design. An orthogonal scheme of L_{25} (3^5) was designed according to Equation (2). Twenty-five impeller models were generated based on the sampling results from the DOE using ANSYS bladegen. Table 2 is the

orthogonal scheme and the meridional shape of the impeller is shown in Figure 2. The position of the inlet profile was adjusted by a Bézier curve with three points.

$$L_m(n^p) \tag{2}$$

Table 1. Range of design variables.

	A	B	C
No	β_{1hub}/°	$\beta_{2middle}$/°	$\beta_{3shroud}$/°
1	17	13	11
2	19	16	14
3	21	18	17
4	23	21	19
5	25	23	21

Table 2. Orthogonal scheme.

	A	B	C		A	B	C
No	β_{1hub}/°	$\beta_{2middle}$/°	$\beta_{3shroud}$/°	*No*	β_{1hub}/°	$\beta_{2middle}$/°	$\beta_{3shroud}$/°
1	17	18	17	14	25	23	17
2	17	16	14	15	19	18	21
3	19	13	17	16	25	16	21
4	21	16	11	17	17	21	19
5	23	16	17	18	17	23	21
6	21	13	21	19	17	13	11
7	21	21	17	20	23	21	21
8	23	18	19	21	25	18	11
9	25	13	19	22	19	23	14
10	19	16	19	23	21	18	14
11	21	23	19	24	23	13	14
12	23	23	11	25	19	21	11
13	25	21	14				

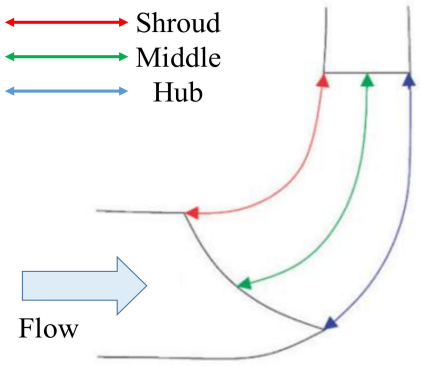

Figure 2. Meridional shape.

2.3. Surrogate Training and Optimum Solution Solving

Artificial neural network (ANN) was used for the surrogate modeling. The concept of ANN and MOGA has been explained in the previous works [13,14]. The Levenberg–Marquardt algorithm was adopted as the training algorithm since it has the fastest convergence rate. Tangent hyperbolic activation function (*tanh*) was applied because it has a much better recognition accuracy for multi-layer neural networks. For this study, a dual-layer feed-forward ANN with 10 hidden neurons was adopted. Figure 3 is the multi-layer feedforward ANN structures used for training the NPSHr objectives.

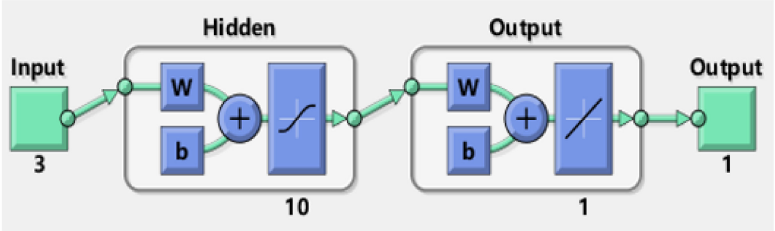

Figure 3. Artificial neural network (ANN) structure for the required net positive suction head (NPSHr) objective.

The mathematical relation for the ANN function is written as Equation (3), the activation function, *tanh* is written as Equation (4) and the linear function as Equation (5).

$$y = g\left(\sum_{j=1}^{n} w_j^2 \times f\left(\sum_{k=1}^{m} w_{k,j}^1 x_k + b_n^1\right)\right) + b^2 \tag{3}$$

$$f(x) = \left[\frac{2}{(1+e^{-2x})}\right] - 1 \tag{4}$$

$$g(x) = ax + b \tag{5}$$

To obtain the global Pareto frontier for the three-objective functions, the multi-objective genetic algorithm was applied to solve the problem. The problem for the three-objective optimization can be described as follows.

$$\begin{cases} find \begin{cases} minimize\ NPSHr\ 0.8Q_d = f_1 \\ NPSHr\ 1.0Q_d = f_2 \\ NPSHr\ 1.2Q_d = f_3 \end{cases} \\ subject\ to \\ 17^\circ \le A \ge 25^\circ \\ 13^\circ \le B \ge 23^\circ \\ 11^\circ \le C \ge 21^\circ \end{cases} \tag{6}$$

Since the problem was a three-objective problem, a 3D Pareto optimal solution was required. In construction of the Pareto solutions, the following input parameters were used. Population size was 200. A 0.8 Pareto-front population and 0.85 crossover fraction were applied with 1000 generations at a function tolerance of 10.

3. Tested Pump and Computational Domain

3.1. Description of Test Pump

The test object is a 250GS40 double-suction centrifugal pump that has a specific speed of 89.5. The flow domain has been divided into the semi-spiral suction domain, a shrouded impeller which has six twisted blades and a volute which also serves as the outlet domain. The test object is shown in Figure 4. Figure 4a shows the computational domain of the volute and suction unit and Figure 4b shows that of the impeller. The design parameters of the pump are presented in Table 3. The specific speed was derived as follows:

$$n_s = 3.65 \times \frac{N \times \sqrt{Q_d}}{60 \times H^{\frac{3}{4}}} \tag{7}$$

where n_s is specific speed, N (rpm) represents rotating speed, Q_d (m^3/h) is the nominal flow rate, and H (m), is the design point head.

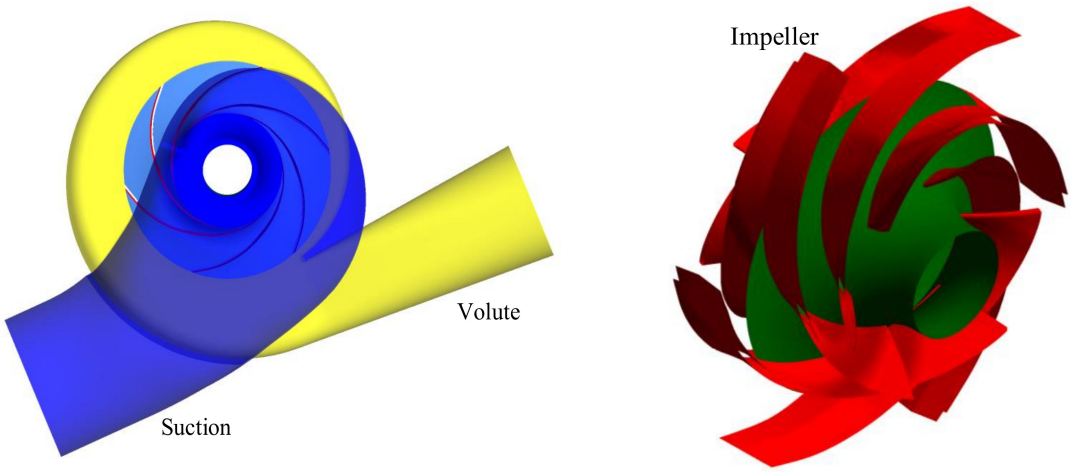

Figure 4. Computational domain of impeller, suction and volute.

Table 3. Design specifications of model pump.

Design Parameters	Value
Nominal flow rate, Q_d (m^3/h)	500
Head, H (m)	40
Rotating speed, N (rpm)	1480
Blade number, z	6
Diameter of suction, D_s (mm)	250
Diameter at impeller inlet, D_1 (mm)	192
Diameter at impeller outlet, D_2 (mm)	365
Diameter of discharge, D_d (mm)	200
Efficiency, η (%)	84
NPSHr (m)	3.5

3.2. NPSHr Prediction Procedure

A novel NPSHr prediction method originally introduced by Ding et al. [19] was applied to speed up the calculation process due to the large sample size of the optimization cases. This new method has been compared with the traditional method of NPSHr prediction using the multi reference frame (MRF) model [20], and further applied to cavitation studies in the double-suction centrifugal pump by Pei [22] and Wang [14]. There are three main prediction steps, and a convergence method, which speeds up to the desired accuracy where convergence is not reached after the third step.

Step 1: The pump head is calculated by introducing a new boundary pair, which is flow rate at the inlet and static pressure at the outlet. The static pressure at the outlet p_{out} is estimated as follows.

$$P_{out}(1) \;=\; H(0) + P_{tot-in}(0) - H_D(0) \;=\; P_{out-in}(0) \tag{8}$$

p_{tot-in} here is the total pressure at the inlet.

Step 2: In step 2 the static pressure at the outlet is calculated to correspond to a 3% drop in the pump head. Here the static pressure is estimate as

$$P_{out}(2) \;=\; 0.97H_{100} - H_D(1) \tag{9}$$

Here, H_{100}, the head at 0% drop in head and H_D is the dynamic head.

Step 3: The third step is to adjust the errors to converge at the 3% head drop. The outlet static pressure for this step is calculated as

$$P_{out}(3) = 0.97H_{100} + P_{tot-in}(2) - H_D(2) \tag{10}$$

Step (n + 1): This step is applied when convergence is not achieved after the third step. This step has been explained in detail by Ding [19] and Pei [20]. Outlet static pressure is calculated as

$$P_{out}(n+1) = 0.97H_{100} + n_3 - H_D(n) \tag{11}$$

3.3. Governing Equations

The time dependent Navier–Stokes equation is derived from the continuity equation [23] is given as

$$\frac{\partial \rho_m}{\partial_t} + \frac{\partial}{\partial x_j}\left(\rho_m u_j\right) = 0 \tag{12}$$

$$\frac{\partial\left(\rho_m u_i u_j\right)}{\partial x_j} + \frac{\partial}{\partial_t}(\rho_m u_i) = \frac{\partial P}{\partial x_i} + \frac{\partial}{\partial x_j}\left[(\mu + \mu_t)\left(\frac{\partial u_i}{\partial x_j} + \frac{\partial u_j}{\partial x_i} + \frac{2}{3}\frac{\partial u_k}{\partial x_k}\delta_{ij}\right)\right] \tag{13}$$

Shear stress transport (SST k-ω) was applied since it has the advantages of both the k-ω and k-ϵ turbulence models [24,25]. To simulate cavitating flows, the equation of mass transport is built from the Rayleigh–Plesset equation, and is expressed as

$$\frac{\partial(\rho_v \alpha_v)}{\partial_t} + \frac{\partial}{\partial x_j}\left(\rho_v \alpha_v u_j\right) = \dot{m} = \dot{m}^+ - \dot{m}^- \tag{14}$$

$$m^+ = C_{vap}\frac{3r_g(1-\alpha_v)\rho_v}{R_b}\sqrt{\frac{2}{3}\frac{max(P_v - P, 0)}{\rho_l}} \tag{15}$$

$$m^- = C_{cond}\frac{3\alpha_v\rho_v}{R_b}\sqrt{\frac{2}{3}\frac{max(P - P_v, 0)}{\rho_l}} \tag{16}$$

From literature, the standardized values are C_{vap} = 50, C_{cond} = 0.01, $r_g = 5 \times 10^{-4}$, $R_b = 10^{-6}$ m, ρ_v = 0.554 kg/m^3, ρ_l = 1000 kg/m^3, and p_v = 3169 Pa [26,27].

3.4. Test of Grid Independence

For maximum simulation accuracy, the test object was meshed using high quality structural hexahedral mesh with ANSYS ICEM. To attain higher precision and boundary motion features, the grids were refined with large numbers and concentrated near the walls. Figure 5 presents an overview of the mesh topology. The volute tongue can be seen in Figure 5a, the impeller in Figure 5b, and suction tongue in Figure 5c. After building the mesh, a test of grid independence was carried out by building 5 independent grids to speed up the calculation time and still maintain accuracy. This was done at the nominal flow condition. It has been established that performance parameters such as head and efficiency are not sufficient enough during the test for grid independence [22,28]; hence, in this research, the influence of the different grid numbers on the volute wall pressure was considered. Monitor points were set in the volute for investigation as shown in Figure 6 and presented in Table 4. The effect of the mesh density on the pump head, efficiency and pressure was least felt at monitor points V1 and V7 as the total mesh number reached 4,266,423. Mesh III was therefore adapted for the numerical simulations to reduce computation load and time. The final mesh has an average Y-plus less than 50, and the distribution can be seen in Figure 7.

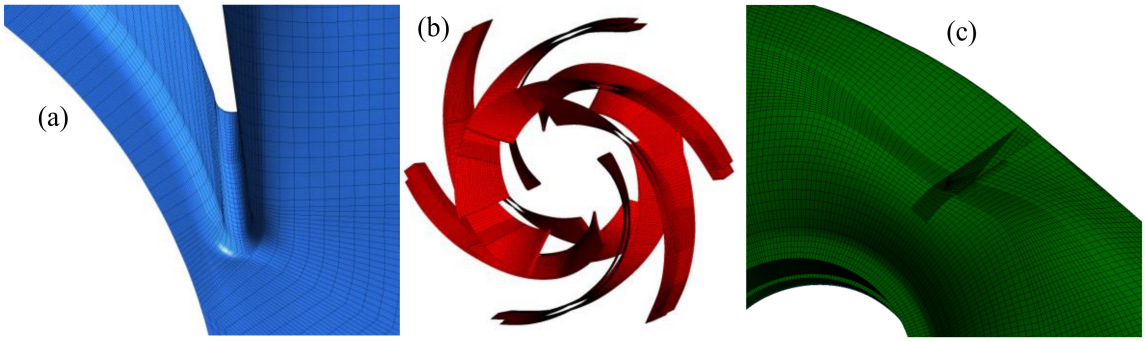

Figure 5. Mesh of calculation domain: (**a**) volute tongue, (**b**) impeller, and (**c**) suction tongue.

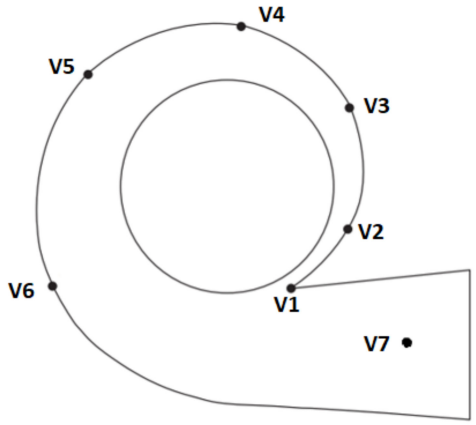

Figure 6. Monitors points in the volute.

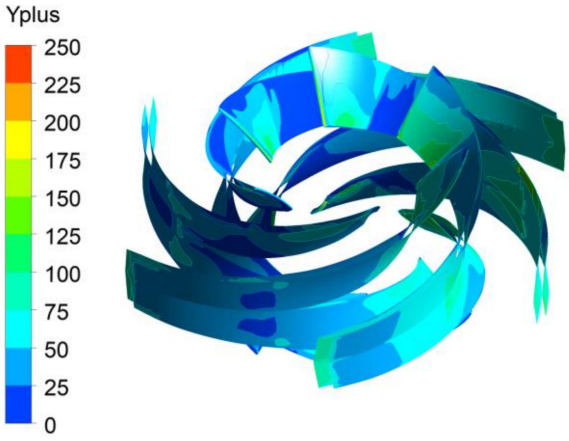

Figure 7. Yplus distribution on blade surface.

Table 4. Grid cells of the selected mesh.

Item		Mesh I	Mesh II	Mesh III	Mesh IV	Mesh V
Ratio	Total Mesh	2,878,243	3,679,342	4,266,423	4,958,168	5,847,757
	H/H_1	1.0000	1.1563	1.2211	1.2201	1.2213
	η/η_1	1.0000	1.1324	1.3043	1.3044	1.3043
	$p_{v1}/p_{v1,1}$	1.0000	1.1520	1.3112	1.3114	1.3111
	$p_{v7}/p_{v7,1}$	1.0000	1.1562	1.2819	1.2822	1.2820

3.5. Numerical Calculation Setup

The computational domain was calculated using ANSYS 2019 R3 to solve the Reynolds-averaged Navier–Stokes equations. Water was used as the working fluid while assuming an isothermal heat

transfer of 25 °C. The SST *(k-ω)* turbulence model was applied since its combined advantages can be extended by the automatic wall treatment to ensure the accuracy of the pressure gradient regardless of the distance to the nearest wall [24,25]. The direction of the flow was set normal to the boundary condition, and a smooth non-slip wall was applied. The default turbulence intensity level of 5% was applied at inlet based on similar works on centrifugal pumps with similar characteristics [14,29]. A high-resolution upwind scheme was applied to ensure accuracy and convergence consistency. At the domain interfaces, a frozen rotor with pitch angle of 360° was set between the rotor and the stator. The boundary conditions were specified as flow rate at inlet and static pressure at the outlet. The Zwart–Gerber–Belamri (ZGB) model was used for cavitation simulations. To determine the convergence criteria, maximum residual values of 10^{-5} were maintained, and iterations had to be periodic stable. Performance indicators were calculated as follows [21].

The Head:

$$H = \frac{P_{tot\text{-}out} - P_{tot\text{-}in}}{\rho g} \tag{17}$$

$p_{tot\text{-}out}$ and $p_{tot\text{-}in}$ are the total pressures at outlet and inlet.

Shaft power:

$$P_s = T\omega \tag{18}$$

T denotes shaft torque while ω, is the angular speed.

Efficiency:

$$\eta = \frac{\rho g H Q}{P_s} \tag{19}$$

3.6. Description of Test System

The experimental test was performed in an open test rig system. Test schematics can be found in Figures 8 and 9 is the experimental setup system. The suction pipe has a diameter of 250 mm while the delivery pipe has a diameter of 200 mm. High precision WT200 pressure transmitters were installed directly in the pipes at the suction and discharge points. The pressure transmitter at the suction end had a measuring range of −0.1 to 0.1 MPa, whereas the outlet transmitter had a measuring range of 0–1.6 MPa. Their measurement uncertainty was 0.5%. The flow rate was measured with LWGY-200A electromagnetic flowmeter with an uncertainty of 0.07%. Hydraulic and cavitation tests were performed at design and non-design flow conditions. To determine the experimental uncertainty, the Type B evaluation was used, and the systematic uncertainty of the experiment was ±0.411%. Further details of the experiments have been provided in our previous studies [20].

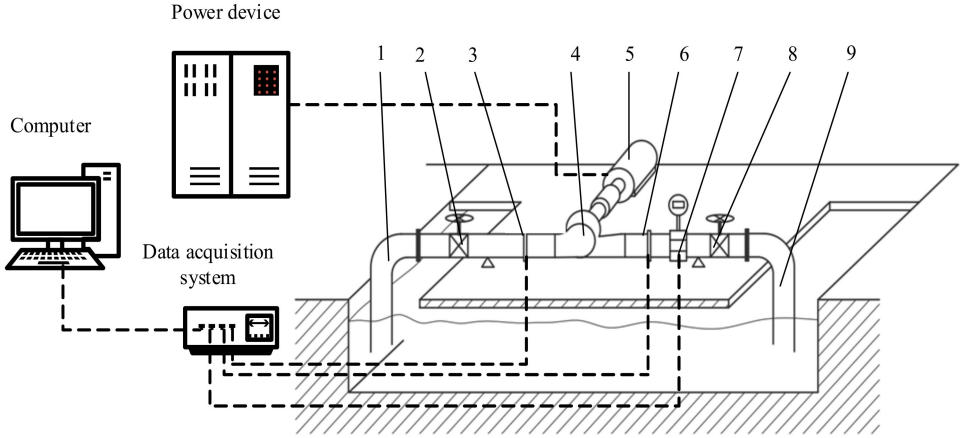

Figure 8. Schematics of the test setup. 1: Inlet pipe, 2(8): Valve, 3(6): Pressure transducer, 4: Tested pump, 5: Driven motor, 7: Magnetic flow meter, and 9: Outlet pipe.

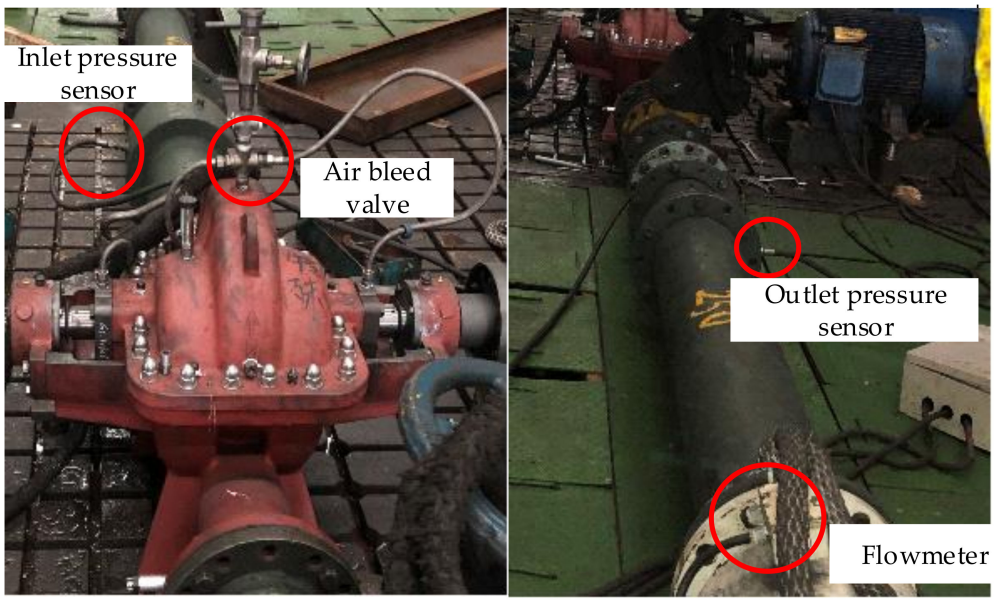

Figure 9. Experimental setup.

4. Discussion of Results

4.1. Validation of Numerical Method

To prove the reliability of the numerical approach, the test results were compared with the computation results and presented in Figure 10. The efficiency curve rose gently from deep part loads to the maximum point of 86.63% at 41.49 m head, and started a steeper decline. The trend was same for both the experiments and numerical results with deviations of 3.01% and 2.03% between the efficiency and head respectively. In the numerical simulations, a smooth wall was assumed. Practically, it is very expensive and difficult to achieve a very smooth surface, and this could account for the minimal deviations between the tests and simulation results. The numerical approach was therefore said to reliable and suitable for the optimization studies since it agreed with the experiments.

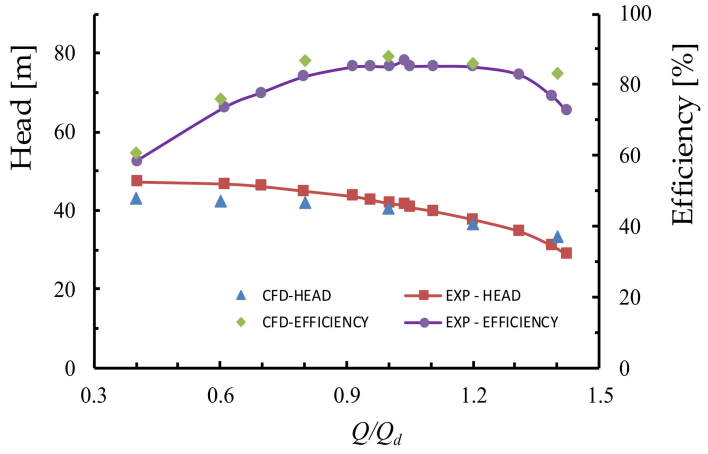

Figure 10. Validation with test results.

4.2. Cavitation Model Validation

The cavitation model was also validated with the test results to further confirm the reliability of the numerical method for cavitation flow simulations. At the nominal flow condition, (Figure 11a), the NPSHr was calculated in only three simulation attempts, which resulted in 3.12% drop in head at NPSHr = 2.628 m. At non-design flow conditions (Figure 11b), the suction performance for the

experimental test was well predicted by the numerical results and the maximum deviation was 4.05%. For all flow conditions, the NPSHr did not exceed the design NPSHr of the pump. At $0.6Q_d$ the computational results were higher than the test values but lower at design and overload conditions. This could also be attributed to the assumption of a smooth non-slip wall during the calculations. The minimum deviations confirm that the cavitation model can be reliable for NPSHr prediction for the optimization studies.

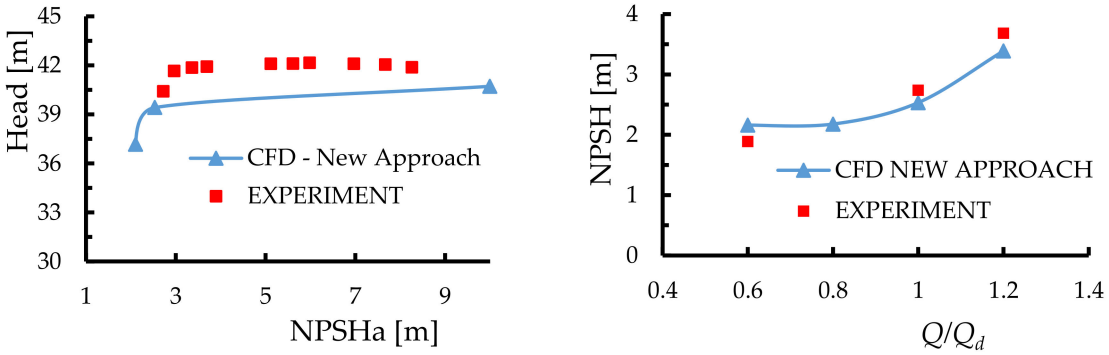

(**a**) Suction performance at design point (**b**) Suction performance at off design points

Figure 11. Comparison of suction performance with test results at design and off design points.

4.3. Results from Optimization Studies

4.3.1. Orthogonal Test Results

The 25 impellers designed from Table 2 were simulated for the three flow conditions. Three of the parameter combinations were invalid. Table 5 gives the upper and lower bounds for the decision variables used for surrogate training, and the results from the orthogonal test is presented in Table 6. From direct analysis, it is observed that, majority of the schemes can satisfy the individual objectives; however, deciding the best scheme from the orthogonal results is difficult. It becomes necessary to apply surrogate models to search for the optimum parameters that would meet the objectives.

Table 5. Boundaries and variables for ANN.

Variables	A	B	C
Upper Bounds	17	13	11
Lower Bounds	25	23	21

4.3.2. Training of Surrogate Model

Artificial neural networks were adopted as the metamodel to build the relationship between the objective functions and decision variables. ANN was then trained to study the relationship between the input and output parameters. The strength of the relationship between the linear model and the dependent variable was determined through R^2 analysis. This determines the suitability of the surrogates for further optimization. Figure 12 shows the R^2 of the ANN models of the objective functions calculated as 0.9877 for $0.8Q_d$ (Figure 12a), 0.9805 for $1.0Q_d$ (Figure 12b), and 0.9759 for $1.2Q_d$ (Figure 12c), indicating that the ANN models for could be applied to the three-objective optimization since the prediction accuracy is high enough. Validation of a surrogate is a requirement hence a comparison of the ANN prediction and the CFD simulation results from Table 6 is drawn in Figures 13–15. From the graphs, the predicted ANN model values are in agreement with the CFD simulation values. The three conditions can all be used as objective functions in the three-objective optimization.

Table 6. Orthogonal scheme results.

Trial No.	β_1/°			NPSHr (m)		
	Hub	Middle	Shroud	$0.8Q_d$	$1.0Q_d$	$1.2Q_d$
1	17	18	17	2.20493	2.47272	3.34366
2	17	16	14	2.242	2.4631	3.5327
3	19	13	17	2.239	2.60439	3.41053
4	21	16	11	2.13633	2.5389	3.49375
5	23	16	17	2.19513	2.49717	3.34304
6	21	13	21	2.32698	2.55007	3.25851
7	21	21	17	2.15205	2.37423	3.20435
9	25	13	19	2.11472	2.44115	3.34089
10	19	16	19	2.15242	2.48385	3.36682
11	21	23	19	2.1968	2.34822	3.12789
12	23	23	11	2.11707	2.46779	3.29704
13	25	21	14	2.19055	2.40843	3.20562
14	25	23	17	2.22882	2.49238	3.19525
15	19	18	21	2.27685	2.37688	3.32605
16	25	16	21	2.16954	2.46852	3.31924
17	17	21	19	2.19175	2.41485	3.21403
18	17	23	21	2.13016	2.49771	3.11064
19	17	13	11	2.11841	2.55672	3.32263
21	25	18	11	2.15538	2.52129	3.41646
22	19	23	14	2.21103	2.41971	3.2512
23	21	18	14	2.18358	2.47889	3.42864
25	19	21	11	2.19366	2.50587	3.49847

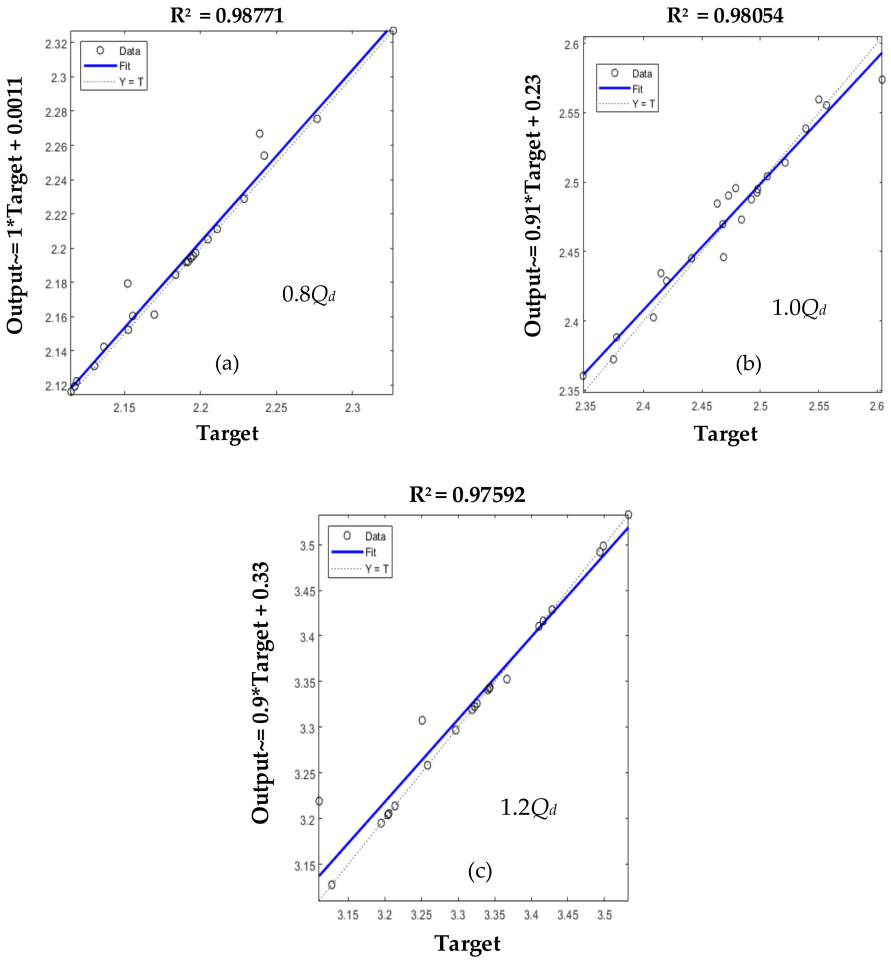

Figure 12. R^2 analysis of NPSHr at $0.8Q_d$, $1.0Q_d$ and $1.2Q_d$.

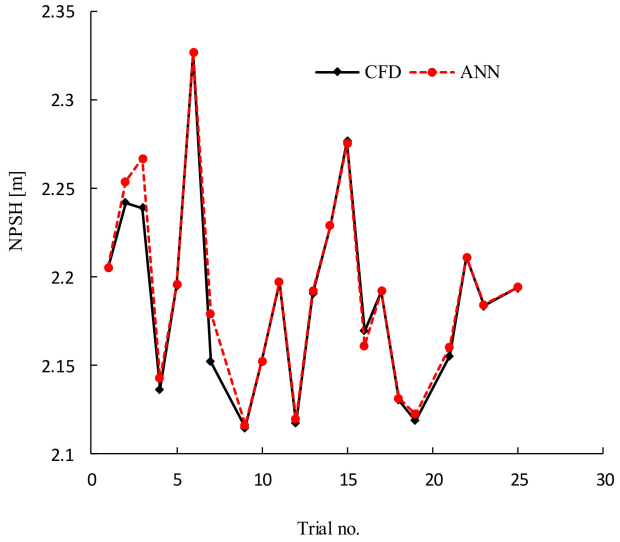

Figure 13. Validation of ANN NPSHr prediction with CFD at $0.8Q_d$.

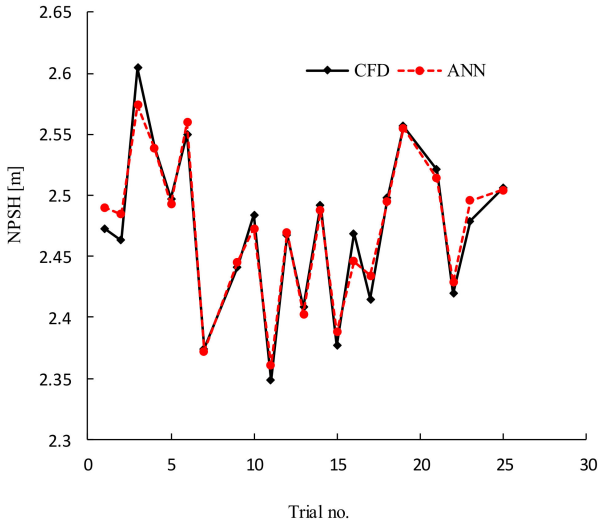

Figure 14. Validation of ANN prediction with CFD at 1.0 Q_d.

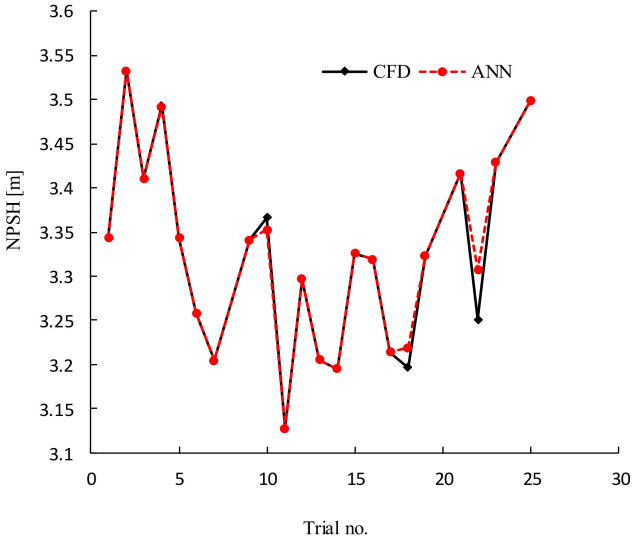

Figure 15. Validation of ANN prediction with CFD at 1.2 Q_d.

4.3.3. Solutions to the Three-Objective Problem

The Pareto frontiers from ANN for the three objective functions have been presented in Figure 16. The optimum solutions were presented as blue points in the Pareto optimum front, and each point represents a model impeller. The Pareto solutions presented a set of 200 optimized impellers schemes that satisfied the optimization objective. Three best impeller schemes were selected and built according to the optimum decision variables in Table 7 and calculated by CFD.

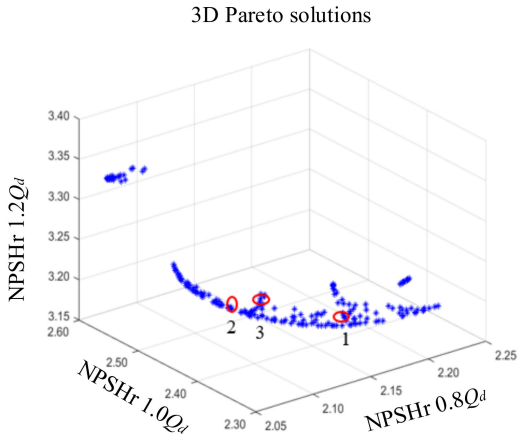

Figure 16. Pareto-frontiers from ANN.

Table 7. Variables for optimum cases.

	A	B	C	Results		
No	β_{1hub}/°	$\beta_{2middle}$/°	$\beta_{3shroud}$/°	**0.8Q_d**	**1.0Q_d**	**1.2Q_d**
1	19.4863	21	16.767	2.108	2.353	3.215
2	19.3992	21	17.262	2.124	2.340	3.210
3	19.3079	21	17.566	2.134	2.334	3.208

Table 8 presents the CFD results from the optimized cases. The CFD predictions were very close to the 3D Pareto predictions rendering the results valid. At part load and design conditions, optimized case 1 performed better than the other cases. At overload condition, optimized case 2 performed better that optimized case 1. For all three cases, optimized case 3 had the worst cavitation performance although the optimization objective was achieved in all cases. Moreover, the head at the design condition was compared for the three flow conditions. Case 3 had the worst head of 38.73 m. Comparing the three cases, the best single case for the optimization objective is case 1. The head comparison at design point is in Table 9.

Table 8. Comparison of original case and best optimal cases.

Name	NPSHr 0.8Q	NPSHr 1.0Q	NPSHr 1.2Q
Original	2.176 m	2.532 m	3.39 m
Case 1	2.089 m	2.358 m	3.271 m
Case 2	2.132 m	2.419 m	3.254 m
Case 3	2.132 m	2.44 m	3.288 m

Table 9. Head comparison at 1.0Q_d.

Name	Head (m)
Original	40.52
Case 1	40.05
Case 2	39.98
Case 3	38.73

4.3.4. Comparison of Suction Performance—Optimized and Original Design

The suction performance of the three optimum cases were compared in Figure 17. In each optimized condition, the results were good. All the three optimum cases performed better, however optimized case 1 performed best at all the flow conditions. At $0.8Q_d$, the effect of the optimization was less for all flow conditions. The selected optimum case was compared with the original model in Figure 18. It was seen that for the original pump, reducing the hub inlet angle from 17° to 16.77° and increasing the hub inlet angle from 15° to 19.49° gave a remarkable improvement of 6.9% in suction performance at $1.0Q_d$. Cavitation performance was improved by 3.5% at overload condition, 4% $0.8Q_d$ and 5% $0.6Q_d$ at non-design conditions. Comparing with the test results the optimization achieved its objective of improving the cavitation performance at non-design points.

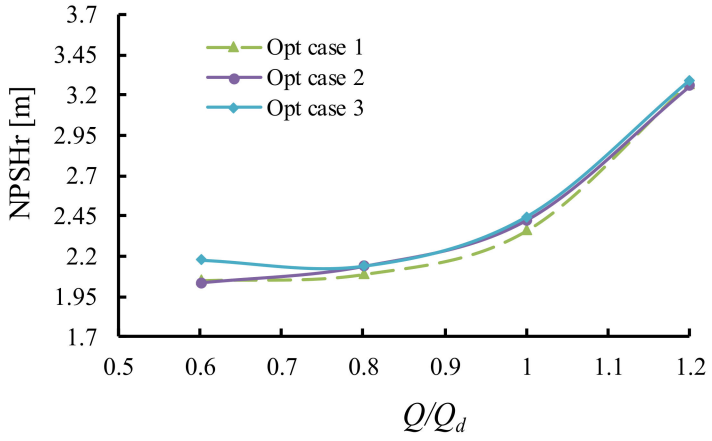

Figure 17. Suction performance of optimized cases and experiments.

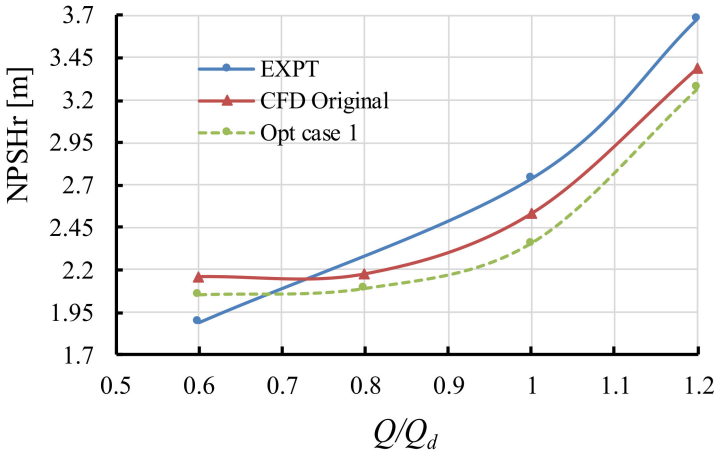

Figure 18. Verification of optimized case 1 with original model.

4.3.5. Internal Flow Analysis

The internal flow of the optimized impeller (case 1) was compared with the original model to reveal the optimization effect on the flow structure. Figure 19 compares the variation of pressure on the blade surface for the three flow conditions that were optimized. At $0.8Q_d$ flow rate, the pressure contour for the original and optimized blades were almost uniform. Looking at the pressure variation the difference was very minimal. At the design condition, the very low pressure areas at the blade leading regions had reduced after optimization. Compared to the original model the low pressure regions covered a wider area than in the optimized model which is an indication that cavitation performance could improve. At overload condition, the low pressure regions within the optimized blade had narrowed as well. The difference was quite clear as compared to the design condition

and part load. The extremely low pressure contours at the leading regions had reduced too. For the three flow conditions, the low pressure distribution on the blade leading regions were reduced after optimization and this can translate to an improvement in suction performance.

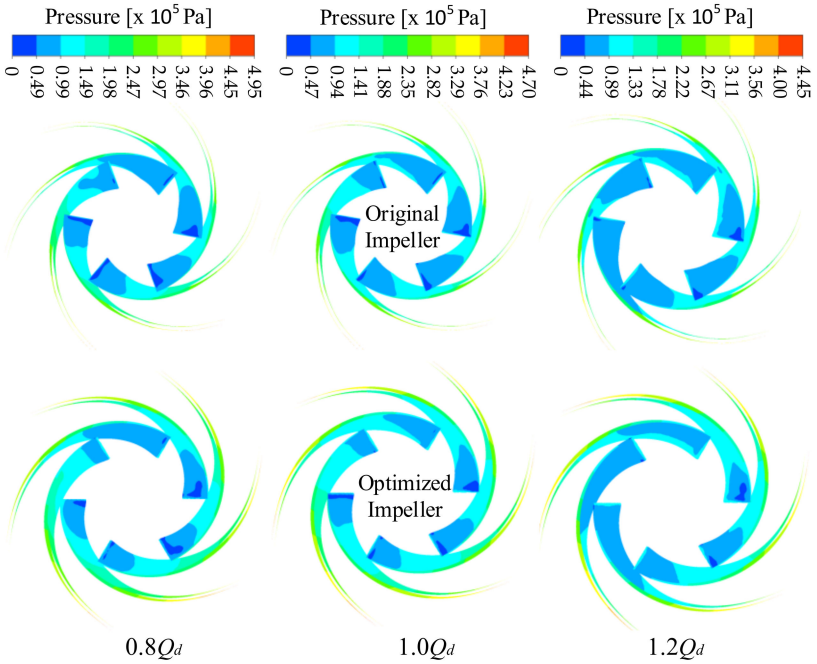

Figure 19. Pressure distribution on blade surface at 0% head drop.

In Figure 20, the pressure fluctuation on the blade surface at critical cavitation conditions were compared. The comparison was done at the critical cavitation point of the original impeller (at NPSH = 2.16 m, NPSH = 2.35 m, and NPSH = 3.16 m), for $0.8Q_d$, $1.0Q_d$, and $1.2Q_d$, respectively. For all the flow conditions, the variation of pressure along the blade surface was improved as compared to the original model. The original model had lower blade surface pressures than the optimized case, indication that suction performance would improve for all the three conditions investigated. The streamline distribution in the impeller flow channel was also analyzed for the various flow conditions in Figure 21 at no cavitation condition. At $0.8Q_d$ part load condition, the flow was distorted in two impeller channels of the original impeller. In one of the channels, some vortex was observed between the leading region and the middle of the impeller. Towards the trailing region the flow separated before normalizing. For the optimized impeller, the flow was uniform, and there was no vortex or separation. The streamline in the channels were uniform in both the original and optimized models at $1.0Q_d$ and $1.2Q_d$, respectively.

4.3.6. Attached Cavity Distribution in the Flow Domain

To clearly see the difference in attached cavity distribution, the critical cavitation point in the original model for each flow rate was used as the reference condition. The cavity distribution in the impeller, suction, and volute of the optimized impeller was compared to the original impeller for that point. Figure 22 is a comparison of the attached cavity distribution in the impeller for different flow conditions. At $0.8Q_d$, the attached cavities in the impeller reduced slightly at NPSH = 2.176, which is the critical cavitation point of the original model. At the design condition, a clear difference was observed. The bubbles covered the entire leading regions in the original impeller. In the optimized model, however, the cavity distribution had reduced, and portions of the leading edge were free from cavitation bubbles at NPSH = 2.53 m. The overload condition was similar to the design condition. Some parts of the leading edge were free from attached cavities; however, the difference in cavity distribution between the two impellers at overload condition was less.

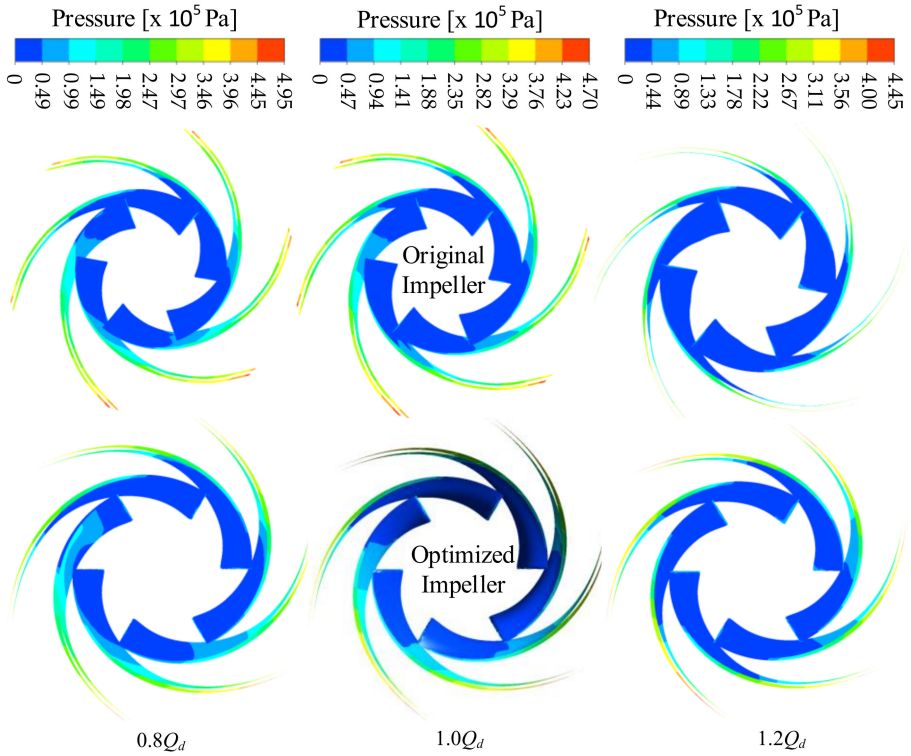

Figure 20. Pressure distribution on blade surface at 3% head drop.

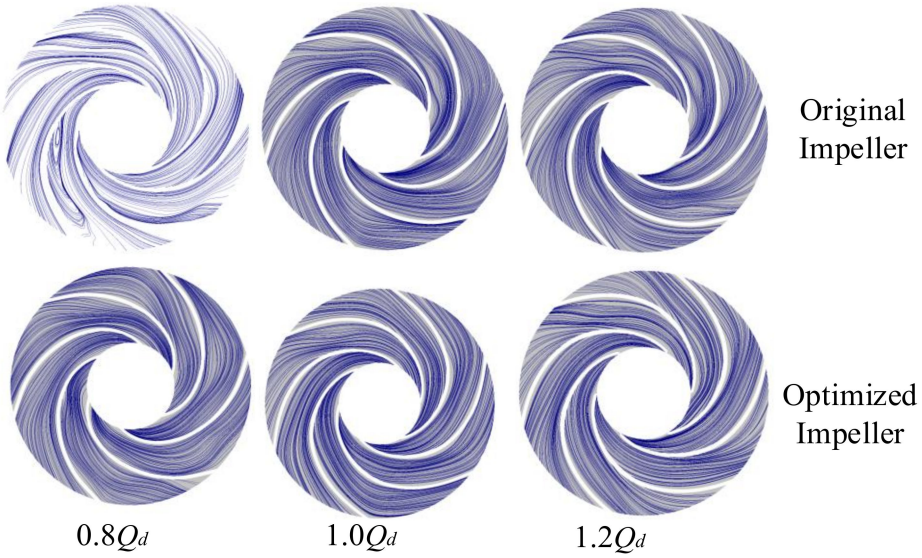

Figure 21. Streamline pattern in impeller channel.

In the suction domain, cavitation occurred around the suction rings. At part load, the attached cavity distribution was not symmetric in both designs. The suction ring at impeller inlet 1 (Figure 4) had cavities made up of bubbles forming around it. It was, however, observed after the optimization that the attached cavities in the suction unit with the optimized impeller had reduced at the critical cavitation point (NPSH = 2.176 m) of the original model. Cavity distribution in the suction at the design point was compared at NPSH = 2.532 m. This was similar to part load condition. Bubbles appeared on suction ring at impeller inlet 1, and there was a reduction in the attached cavities around the suction ring. For 1.2Q_d, the original impeller had bubbles on both rings. In the optimized model, the cavities had reduced to a single suction ring when the comparison was done at NPSH = 3.39 m. Only the suction ring at impeller inlet 2 had attached cavity distributions. Generally, there was reduction in

cavitation bubbles for all flow conditions. This meant that the suction performance had improved for all three conditions and the optimization target has been achieved. Figure 23 shows the bubble distribution in the suction domain.

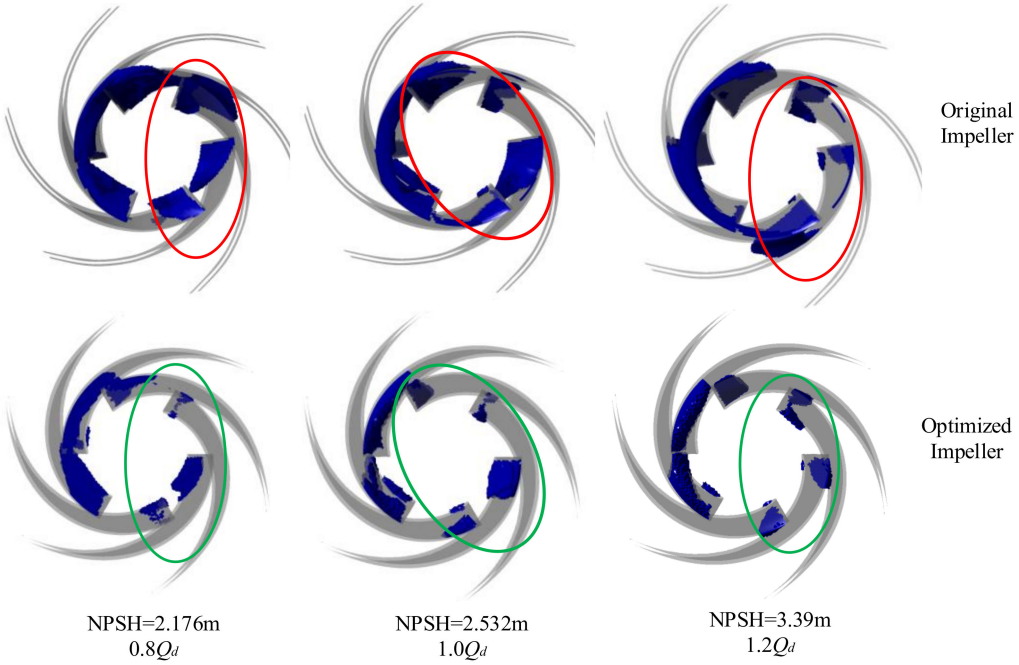

Figure 22. Bubble distribution in the impeller.

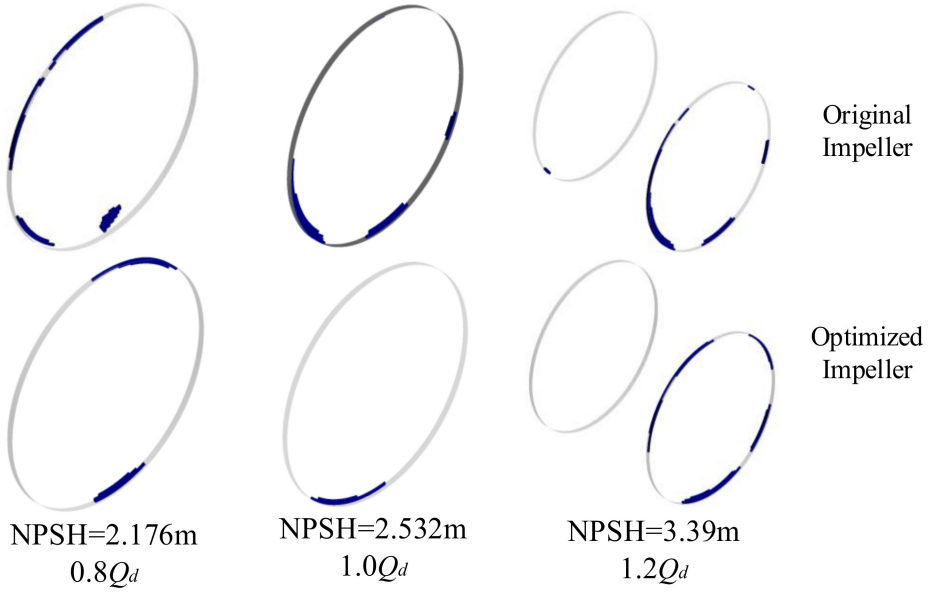

Figure 23. Attached cavity distribution in the suction.

5. Conclusions

Cavitation has been a treat to cooling water circulation pumps leading to reduced efficiency and damage of pump impellers. Hence, to improve the anti-cavitation performance and ensure longer life and reliability of cooling water circulation pumps, a multi-parameter and a multi-condition optimization approach was designed. In the optimization design, a dual-layer feedforward artificial neural network and genetic algorithm was then applied to improve the cavitation performance of the double-suction impeller over a wider range of operating conditions. The results from the study are as follows:

1. For the best case, there was a 6.9% improvement of suction performance at the design point. At non-design flow conditions, the cavitation performance was improved by 3.5% at $1.2Q_d$ overload condition, 4% at $0.8Q_d$, and 5% at $0.6Q_d$.
2. The pressure distribution on the blade was improved compared to the original model, and the streamline at $0.8Q_d$ was improved also.
3. The attached cavity distribution in the impeller and suction were lower than the original model when they were compared at NPSH = 2.176 m for $0.8Q_d$, at NPSH = 2.532 m for the nominal flow condition, and at NPSH = 3.36 m overload condition of $1.2Q_d$.
4. Finally, in this optimization, the suction performance of the double-suction centrifugal pump was improved at non-design flow conditions using a faster method for cavitation flow simulations. This can serve as a theoretical reference for pump optimization design against cavitation.

Author Contributions: Conceptualization, W.W. and Y.L.; methodology, M.K.O. and S.Y.; software, M.K.O.; validation, J.L. and B.Z.; formal analysis, W.W., Y.L., M.K.O., and B.Z.; writing—original draft preparation, M.K.O.; writing—review and editing, M.K.O. and W.W.; and project administration, S.Y. All authors have read and agreed to the published version of the manuscript.

Funding: This work is supported by the Natural Science Foundation of Jiangsu Province (Grant No. BK20190851), Primary Research & Development Plan of Shandong Province (Grant No. 2019TSLH0304), Natural Science Foundation of China (Grant No. 51879121, 51579104) and Primary Research & Development Plan of Jiangsu Province (Grant No. BE2019009-1).

Conflicts of Interest: The authors declare no conflict of interest.

References

1. Osman, M.K.; Wang, W.; Yuan, J.; Zhao, J.; Wang, Y.; Liu, J. Flow loss analysis of a two-stage axially split centrifugal pump with double inlet under different channel designs. *Proc. Inst. Mech. Eng. Part C J. Mech. Eng. Sci.* **2019**, *233*, 5316–5328. [CrossRef]
2. Pei, J.; Wang, W.; Pavesi, G.; Osman, M.K.; Meng, F. Experimental investigation of the nonlinear pressure fluctuations in a residual heat removal pump. *Ann. Nucl. Energy* **2019**, *131*, 63–79. [CrossRef]
3. Kang, C.; Mao, N.; Zhang, W.; Gu, Y. The influence of blade configuration on cavitation performance of a condensate pump. *Ann. Nucl. Energy* **2017**, *110*, 789–797. [CrossRef]
4. Wei, Z.; Yang, W.; Xiao, R. Pressure Fluctuation and Flow Characteristics in a Two-Stage Double-Suction Centrifugal Pump. *Symmetry* **2019**, *11*, 65. [CrossRef]
5. Tani, N.; Yamanishi, N.; Tsujimoto, Y. Influence of flow coefficient and flow structure on rotational cavitation in inducer. *J. Fluids Eng.* **2012**, *134*, 021302. [CrossRef]
6. Kobayashi, K.; Chiba, Y. Numerical simulation of cavitating flow in mixed flow pump with closed type impeller. In Proceedings of the ASME 2009 Fluids Engineering Division Summer Meeting, Vail, CO, USA, 2–6 August 2009; pp. 339–347.
7. Li, X.; Yuan, S.; Pan, Z.; Yuan, J.; Fu, Y. Numerical simulation of leading edge cavitation within the whole flow passage of a centrifugal pump. *Sci. China Technol. Sci.* **2013**, *56*, 2156–2162. [CrossRef]
8. Fu, Q.; Zhang, F.; Zhu, R.; He, B. A systematic investigation on flow characteristics of impeller passage in a nuclear centrifugal pump under cavitation state. *Ann. Nucl. Energy* **2016**, *97*, 190–197. [CrossRef]
9. Pei, J.; Yin, T.; Yuan, S.; Wang, W.; Wang, J. Cavitation optimization for a centrifugal pump impeller by using orthogonal design of experiment. *Chin. J. Mech. Eng.* **2017**, *30*, 103–109. [CrossRef]
10. Dönmez, A.H.; Yumurtacı, Z.; Kavurmacıoğlu, L. The Effect of Inlet Blade Angle Variation on Cavitation Performance of a Centrifugal Pump: A Parametric Study. *J. Fluids Eng.* **2018**, *141*, 021101. [CrossRef]
11. Bonaiuti, D.; Zangeneh, M.; Aartojarvi, R.; Eriksson, J. Parametric Design of a Waterjet Pump by Means of Inverse Design, CFD Calculations and Experimental Analyses. *J. Fluids Eng.* **2010**, *132*, 031104. [CrossRef]
12. Xu, Y.; Tan, L.; Cao, S.; Qu, W. Multiparameter and multiobjective optimization design of centrifugal pump based on orthogonal method. *Proc. Inst. Mech. Eng. Part C J. Mech. Eng. Sci.* **2017**, *231*, 2569–2579. [CrossRef]
13. Pei, J.; Gan, X.; Wang, W.; Yuan, S.; Tang, Y. Multi-objective Shape Optimization on the Inlet Pipe of a Vertical Inline Pump. *J. Fluids Eng.* **2019**. [CrossRef]

14. Wang, W.; Osman, M.K.; Pei, J.; Gan, X.; Yin, T. Artificial Neural Networks Approach for a Multi-Objective Cavitation Optimization Design in a Double-Suction Centrifugal Pump. *Processes* **2019**, *7*, 246. [CrossRef]
15. Jin, R.; Wei, C.; Simpson, T.W. Comparative studies of metamodelling techniques under multiple modelling criteria. *Struct. Multidiscip. Optim.* **2001**, *23*, 1–13. [CrossRef]
16. Wang, W.; Pei, J.; Yuan, S.; Zhang, J.; Yuan, J.; Xu, C. Application of different surrogate models on the optimization of centrifugal pump. *J. Mech. Sci. Technol.* **2016**, *30*, 567–574. [CrossRef]
17. Pei, J.; Wang, W.; Osman, M.K.; Gan, X. Multiparameter optimization for the nonlinear performance improvement of centrifugal pumps using a multilayer neural network. *J. Mech. Sci. Technol.* **2019**, *33*, 2681–2691. [CrossRef]
18. Tao, R.; Xiao, R.; Zhu, D.; Wang, F. Multi-objective optimization of double suction centrifugal pump. *Proc. Inst. Mech. Eng. Part C J. Mech. Eng. Sci.* **2018**, *232*, 1108–1117. [CrossRef]
19. Ding, H.; Visser, F.; Jiang, Y. A practical approach to speed up NPSHR prediction of centrifugal pumps using CFD cavitation model. In Proceedings of the ASME 2012 Fluids Engineering Division Summer Meeting collocated with the ASME 2012 Heat Transfer Summer Conference and the ASME 2012 10th International Conference on Nanochannels, Microchannels, and Minichannels, Rio Grande, PR, USA, 8–12 July 2012; pp. 505–514.
20. Pei, J.; Osman, M.K.; Wang, W.; Appiah, D.; Yin, T.; Deng, Q. A Practical Method for Speeding up the Cavitation Prediction in an Industrial Double-Suction Centrifugal Pump. *Energies* **2019**, *12*, 2088. [CrossRef]
21. Gülich, J.F. *Centrifugal Pumps*; Springer: Berlin/Heidelberg, Germany, 2010.
22. Pei, J.; Osman, M.K.; Wang, W.; Yuan, J.; Yin, T.; Appiah, D. Unsteady flow characteristics and cavitation prediction in the double-suction centrifugal pump using a novel approach. *Proc. Inst. Mech. Eng. Part A J. Power Energy* **2020**, *234*, 283–299. [CrossRef]
23. Medvitz, R.B.; Kunz, R.F.; Boger, D.A.; Lindau, J.W.; Yocum, A.M.; Pauley, L.L. Performance analysis of cavitating flow in centrifugal pumps using multiphase CFD. *J. Fluids Eng.* **2002**, *124*, 377–383. [CrossRef]
24. Menter, F.R. Two-equation eddy-viscosity turbulence models for engineering applications. *AIAA J.* **1994**, *32*, 1598–1605. [CrossRef]
25. Bardina, J.; Huang, P.; Coakley, T.; Bardina, J.; Huang, P.; Coakley, T. Turbulence modeling validation. In Proceedings of the 28th Fluid Dynamics Conference, Snowmass Village, CO, USA, 29 June–2 July 1997; p. 2121.
26. Zwart, P.J.; Gerber, A.G.; Belamri, T. A two-phase flow model for predicting cavitation dynamics. In Proceedings of the Fifth International Conference on Multiphase Flow, Yokohama, Japan, 30 May–3 June 2004.
27. Mejri, I.; Bakir, F.; Rey, R.; Belamri, T. Comparison of computational results obtained from a homogeneous cavitation model with experimental investigations of three inducers. *J. Fluids Eng.* **2006**, *128*, 1308–1323. [CrossRef]
28. Pei, J.; Zhang, F.; Appiah, D.; Hu, B.; Yuan, S.; Chen, K.; Asomani, S. Performance Prediction Based on Effects of Wrapping Angle of a Side Channel Pump. *Energies* **2019**, *12*, 139. [CrossRef]
29. Tang, X.; Zou, M.; Wang, F.; Li, X.; Shi, X. Comprehensive Numerical Investigations of Unsteady Internal Flows and Cavitation Characteristics in Double-Suction Centrifugal Pump. *Math. Probl. Eng.* **2017**, *2017*, 1–13. [CrossRef]